Prashant L. Suryawanshi, Shirish H. Sonawane*, Bharat A. Bhanvase, Muthupandian Ashokkumar, Makarand S. Pimplapure and Parag R. Gogate

Synthesis of iron oxide nanoparticles in a continuous flow spiral microreactor and Corning® advanced flow™ reactor

DOI 10.1515/gps-2016-0138
Received August 15, 2016; accepted January 3, 2017; previously published online March 4, 2017

Abstract: In the present work, synthesis of iron oxide nanoparticles (NPs) using continuous flow microreactor (MR) and advanced flow™ reactor (AFR™) has been investigated with evaluation of the efficacy of the two types of MRs. Effect of the different operating parameters on the characteristics of the obtained NPs has also been investigated. The synthesis of iron oxide NPs was based on the co-precipitation and reduction reactions using iron (III) nitrate precursor and sodium hydroxide as reducing agents. The iron oxide NPs were characterized using transmission electron microscopy (TEM), Fourier transform infrared spectroscopy, and X-ray diffraction (XRD) analysis. The mean particle size of the obtained NPs was less than 10 nm at all flow rates (over the range of 20–60 ml/h) in the case of spiral MR, while, in the case of AFR™, the particle size of NPs was below 20 nm with no specific trend observed with the operating flow rates. The XRD and TEM analyses of iron oxide NPs confirmed the crystalline nature and nanometer size range, respectively. Further, magnetic properties of the synthesized iron oxide NPs were studied using electron spin resonance spectroscopy; the resonance absorption peak shows the *g*-factor values as 2.055 and 2.034 corresponding to the magnetic fields of 319.28 and 322.59 mT for MR and AFR™, respectively.

***Corresponding author: Shirish H. Sonawane,** Department of Chemical Engineering, National Institute of Technology, Warangal-506004, Telangana, India, e-mail: shirish@nitw.ac.in
Prashant L. Suryawanshi: Department of Chemical Engineering, National Institute of Technology, Warangal-506004, Telangana, India
Bharat A. Bhanvase: Chemical Engineering Department, Laxminarayan Institute of Technology, Rashtrasant Tukadoji Maharaj Nagpur University, Nagpur 440033, MS, India
Muthupandian Ashokkumar: School of Chemistry, University of Melbourne, VIC 3010, Australia
Makarand S. Pimplapure: Corning Technologies India Pvt. Ltd., Gurgaon 122002, India
Parag R. Gogate: Chemical Engineering Department, Institute of Chemical Technology, Mumbai 400019, MS, India

Keywords: advanced flow reactor (AFR™); co-precipitation; iron oxide nanoparticles; microreactor (MR); particle size distribution (PSD).

1 Introduction

Over the past decade, research related to the synthesis and modification of nanoparticles (NPs) has made a great impact on material engineering and surface science applications attributed to the unique chemical and physical properties for the NPs as compared to the bulk materials [1]. The colloidal NPs have applications in a variety of fields including biosensors, catalysis, targeted drug delivery system, detection of genes, conducting inks, magnetic resonance imaging, energy storage devices such as fuel cells, batteries etc., medical diagnostics, and antimicrobial agents [2–13]. In recent years, interest in the efficient synthesis of magnetic iron oxide NPs has increased significantly due to the wide range of applications in the field of magnetic storage devices, chemical processing industries, biotechnology, water purification, and biomedical applications like thermal therapy, chemotherapy, diagnostic magnetic resonance imaging, magnetofection, and drug delivery [12–21]. The common forms of iron oxide generally found are maghemite (γ-Fe_2O_3), hematite (α-Fe_2O_3), magnetite (Fe_3O_4), and oxo-hydroxide (FeOOH) [22, 23]. Yuvakkumar et al. [24] prepared nano-scaled zero valent iron (50–100 nm) using the reduction method based on the use of ferric ions and sodium borohydride in ethanol under atmospheric conditions. Behera et al. [25] also prepared iron oxide NPs for antibacterial applications using co-precipitation method. Lee et al. [26] investigated the synthesis of iron oxide nanomaterials in microfluidics device under ambient conditions with the use of co-precipitation method. The reported particle size of iron oxide NPs was less than 10 nm with applications explored in the biomedical fields. Shahane et al. [27] used low temperature co-precipitation method for the synthesis of superparamagnetic Fe_3O_4 NPs for ferrofluids application. It was reported that the nanocrystalline sizes of 11.5 and

20 nm were obtained before and after annealing as confirmed using the X-ray diffraction (XRD) and transmission electron microscopy (TEM) analysis. Azimi et al. [28] studied the formation of the magnetically excited NPs and reported particle size in the range of 10.5–25 nm for the case of Y-type micromixer at conditions of flow rate of 2–30 ml/min. The synthesized NPs were reported to give significant enhancement in the mass transfer coefficient and extraction efficiency. The present work deals with synthesis of colloidal iron oxide NPs using co-precipitation and reduction method using the continuous flow spiral copper wire microreactor (MR) and Corning® advanced flow™ reactor (AFR™). It is important to understand that both MR and AFR offer several advantages over the conventional reactors. The significantly higher surface to volume ratio in the case of both MR [7, 29] and AFR™ [30, 31], which is a patented technology of Corning industry, is responsible for the improvement in heat and mass transfer rates in comparison with conventional reactors such as continuous stirred tank reactor, plug flow reactor, and batch reactor [32]. Also, efficient heat management and mixing can be achieved due to smaller reaction volume especially important for the efficient synthesis of colloidal iron oxide NPs. Small-scale channels in AFR reactor and MRs offer advantages such as safety, scale up, mixing quality, heat management, and improved yield over the classical batch approach [33–35]. In addition, the desired reactions can be completed in MR and AFR™ within much lower time (in second or even few milliseconds). Based on these advantages, MR and AFR™ were used for the synthesis of magnetic iron NPs based on the use of iron (III) nitrate and sodium hydroxide. The effect of various operating conditions on the particle characteristics in terms of the size, morphology and distribution as well as elemental composition has been investigated. The selection of the iron oxide NPs as the model system is justified based on the number of important applications in the field of catalysis, pigments, electronic energy devices (like lithium ion batteries, fuel cell), medical/biomedical applications (like diagnostics magnetic resonance imaging, drug delivery, targeted thermos-sensitive chemotherapy, and cancer treatment), wastewater treatment, etc. [14–16, 36–49].

2 Materials and methods

2.1 Materials

For the synthesis of colloidal NPs, iron (III) nitrate nonahydrate [$Fe(NO_3)_3.9H_2O$, analytical grade], procured from Merck Specialities Pvt. Ltd., Mumbai, India, was used as a precursor. Sodium hydroxide (NaOH) was procured from MOLYCHEM, Mumbai, India. N-Cetyl trimethyl ammonium bromide (CTAB, $C_{19}H_{42}BrN$, analytical grade) was procured from Sisco Laboratory Pvt. Ltd. Mumbai, India. All the procured chemicals were with specified purity of above 98% and used as received from the supplier. Distilled water, prepared in the laboratory freshly, was used for the preparations of various solutions used during the experiments.

2.2 Microreactor assembly

Copper tube with 800 μm inner diameter and 1240 mm length was used for the fabrication of low-cost inhouse MR system (Figure 1A**)**. The copper tube was arranged spirally with 6 turns of 200 mm diameter for each loop. The spirally wound tube was provided with Y-type microchannel for the injection of the reagents with the help of syringe pumps (Scientech Tech. Pvt. Ltd., Pune, India). The schematic representation of the experimental setup based on spiral copper tube MR has been shown in Figure 1A.

2.3 Synthesis of stable colloidal iron oxide nanoparticles in spiral copper tube microreactor

Initially, homogeneous solutions of desired concentration of iron (III) nitrate nonahydrates [$Fe(NO_3)_3.9H_2O$] and sodium hydroxide (NaOH) as given in Table 1 were prepared in distilled water at temperature of 25°C ± 2°C. CTAB surfactant having critical micelle concentration of 1 mM/l was added into the solutions of both reagents [50, 51]. $Fe(NO_3)_3.9H_2O$ and NaOH solutions were fed to the reactor, with the use of syringe, separately at temperature of 25°C ± 2°C through Y-type micromixer connected on the feed side of the MR (Figure 1A). The product was collected from the other side of the MR. The flow rates of $Fe(NO_3)_3.9H_2O$ and NaOH solutions were varied over the range of 20–60 ml/h, with the help of syringe pumps during synthesis of iron oxide NPs in the spiral MR. The molar ratio of reductant to precursor was maintained constant at 1 : 1 for all experiments as given in Table 1.

2.4 Synthesis of stable colloidal iron oxide nanoparticles in Corning AFR™

Synthesis of stable colloidal iron oxide NPs was also achieved in the Corning AFR™ which typically contains two heart-shaped modules. Each module has dimensions of 77 mm × 62 mm and is made up of ceramic with a maximum capacity of 0.45 ml. Two modules of AFR™ were used in order to maintain the required residence time of the reactants in the reactor. The total volume capacity of two modules with the given mixing length is 1 ml. Two syringe pumps were used to feed the reactant solutions in AFR™ system. Aqueous solutions of iron (III) nitrate nonahydrate and sodium hydroxide of desired concentrations (Table 1) with surfactant (CTAB) added in both solutions, were fed to the AFR™. The reaction mixture was maintained at a constant temperature of 25°C ± 2°C during the course of the reaction. Teflon tubing was used for the interconnection of syringes with AFR™. During the passage through the reactor, iron (III) nitrate nonahydrate is reduced by sodium hydroxide resulting in the formation of reduced

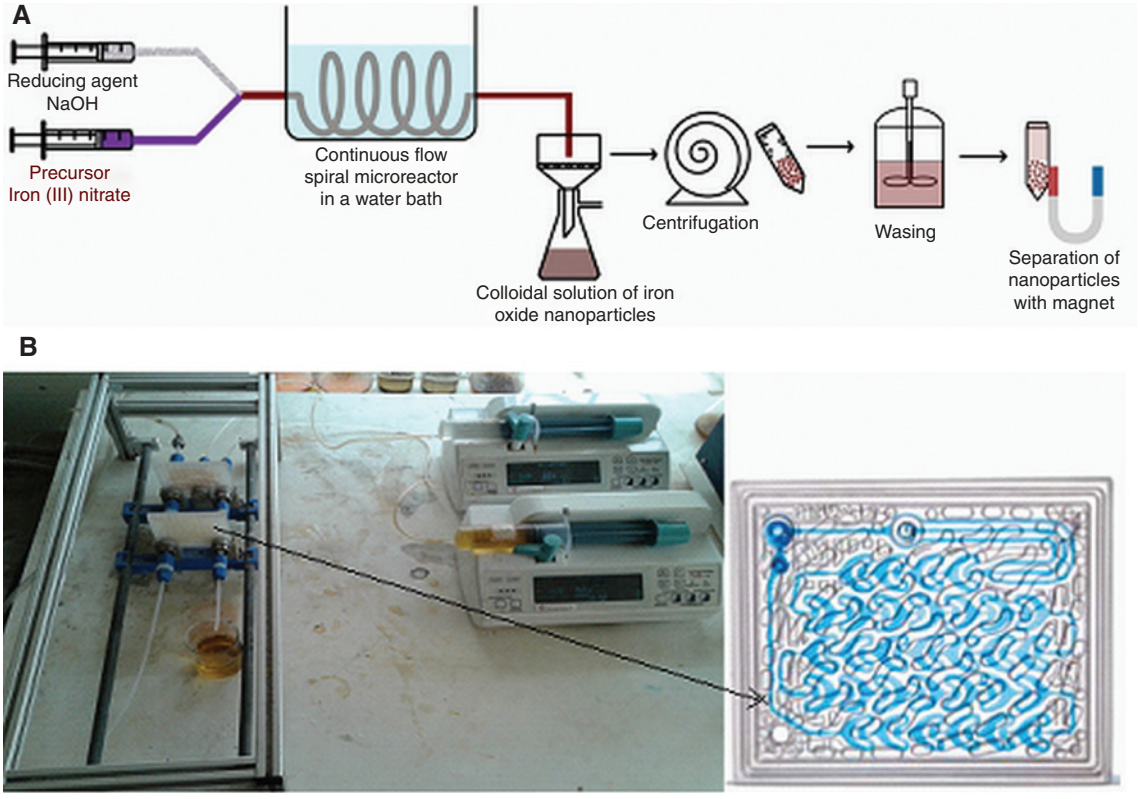

Figure 1: Schematic diagram of (A) experimental set up with fabricated microreactor (MR) and (B) experimental set up of advanced flow reactor™ (AFR™) for the synthesis of magnetic iron oxide nanoparticles (NPs).

Table 1: Different conditions of reagents and flow rates used in the synthesis as well as the results for particle size distribution for the obtained colloidal iron oxide nanoparticles in microreactor and advanced flow reactor.

Concentration			Flow rate (ml/h)	Synthesis in microreactor			Synthesis in AFR™		
$Fe(NO_3)$(M)	NaOH (M)	CTAB		Residence time (min)	Particle size (nm)	Zeta potential (mV)	Residence time (min)	Particle size (nm)	Zeta potential (mV)
0.1	0.1	0.005	60	0.62	6.3	14.6	1	10.5	0.0462
0.1	0.1	0.005	50	0.75	9.11	20.5	1.2	6.64	14.4
0.1	0.1	0.005	40	0.94	9.21	42.1	1.5	15.5	22.0
0.1	0.1	0.005	30	1.25	9.8	37.2	2	10.92	4.60
0.1	0.1	0.005	20	1.87	9.01	−0.06	3	18.19	0.0806

iron, which is subsequently stabilized into iron oxide NPs. The experimental conditions used during the synthesis of iron oxide NPs using AFR™ have been reported in Table 1. The flow rates of $Fe(NO_3)_3.9H_2O$ and NaOH solutions were varied over the range 20–60 ml/h with the help of syringe pumps. The molar ratio of the reductant to precursor was again maintained constant at 1:1 for all the experiments. The problem of agglomeration was observed at lower flow rates and higher precursor concentration during experiments performed in AFR™. Therefore, higher flow rates of precursor solutions with lower concentrations were preferred in AFR™. At lower flow rates, the residence time of the reactant is higher, which leads to the formation of more iron oxide NPs inside the AFR™ giving clogging in the reactor. It was also observed that the specific heart shape design of AFR™ cannot handle the quick formation of larger size particles and hence, it is undesirable to use the higher feed concentration and higher molecular weight or long chain polymeric surfactant molecules in this type of reactor. The schematic representation of the experimental setup for the synthesis of iron oxide NPs in AFR™ has been depicted in Figure 1B.

2.5 Characterization

The particle size distribution (PSD) and zeta potential analysis were performed in order to establish the size distribution of particles and stability of colloidal suspension based on dynamic light scattering technique, respectively. For the analysis of zeta potential, Malvern

Nano-Series Zeta sizer (ZS90, Malvern Instrument) has been used. UV-visible absorption spectra of the iron oxide NPs obtained at different experimental conditions were recorded using UV-Vis Spectrophotometer (Shimadzu UV 1800). Fourier transform infrared (FTIR) analysis of the NPs was also performed using a Shimadzu 8400 model FTIR spectrometer. The morphological and structural properties of the obtained NPs were established using the Transmission Electron Microscopy analyzer (PHILIP, CM200 model) and XRD analyzer (PANalytical, X'Pert-PRO diffractometer). The XRD analysis was performed using a Cu Kα source ($\lambda = 1.540598$ Å). Magnetic properties and magnetization dynamic behavior of iron oxide (Fe_2O_3) NPs were also analyzed using the electron spin resonance (ESR) analysis based on the use of Bruker ESP300 spectrometer equipped with the X-type band at an applied power of 1 mW, sweep time of 30 s, and microwave frequency of 9.185 GHz at a constant temperature of 25°C ± 3°C.

3 Results and discussion

3.1 Reaction mechanism for the formation of iron oxide nanoparticles

The overall precipitation cum reduction reaction governing the formation of iron oxide NPs occurring in both the reactors is as follows:

$$Fe(NO_3)_3.9H_2O_{(aq.)} + 3NaOH_{(aq.)} \rightarrow Fe(OH)_{3(s)} \downarrow + 3NaNO_{3(aq.)} + 9H_2O \quad (1)$$

During the reaction, $Fe(NO_3)_3.9H_2O$ gets dissociated into Fe^{3+} and NO_3^- ions in distilled water. Similarly, NaOH gets dissociated into Na^+ and OH^- ions. The complete ionic reaction mechanism can be written as follows:

$$Fe^{3+}_{(aq.)} + 3NO^-_{3\ (aq.)} + 3Na^+_{(aq.)} + 3OH^-_{(aq.)} \rightarrow Fe(OH)_{3(s)} \downarrow + 3Na^+_{(aq.)} + 3NO^-_{3\ (aq.)} \quad (2)$$

Subsequently the formation of iron oxide occurs as per the following reaction:

$$2Fe(OH)_{3(s)} \rightarrow Fe_2O_{3(s)} + 3H_2O \quad (3)$$

In the spiral copper tube MR and AFR™, co-precipitation cum reduction reaction is probably the simplest and most efficient chemical pathway to obtain iron oxide NPs. Iron oxides (either magnetite Fe_3O_4 or maghemite γ-Fe_2O_3) are usually formed by adding an aqueous solution of base to an aging stoichiometric mixture of ferrous and ferric salts at room temperature [52]. The overall formation of iron oxide NPs by co-precipitation and reduction reaction in the MR and AFR™ is generally controlled by the following two steps: (1) the precursors obtained by precipitation reaction are required for the nucleation and crystallization and (2) the direct formation of a metal oxide [25, 26, 52].

3.2 Iron oxide nanoparticles formation in MR and AFR

Colloidal iron oxide NPs were prepared under conditions of different flow rates at constant temperature of the reaction medium as 25°C ± 1°C in MR maintained with the help of water bath. The reductant to precursor molar ratio was maintained at 1 : 1 and the product obtained was yellowish brown in color. Figure 2A,B shows the UV absorption spectra of the obtained iron oxide NPs in the presence of the surfactant (CTAB) at different flow rates in MR and AFR, respectively. It can be seen from the figure that the λ_{max} value was in between 470 and 480 nm. An increase in the flow rate gives a corresponding increase in the absorption value, which indicates the formation of a large number of iron oxide NPs in the MR. With an increase in the flow rate, decrease in the residence time occurs and hence there is no appreciable growth of the NPs resulting in smaller particles in MR (Figure 2A). Due to this

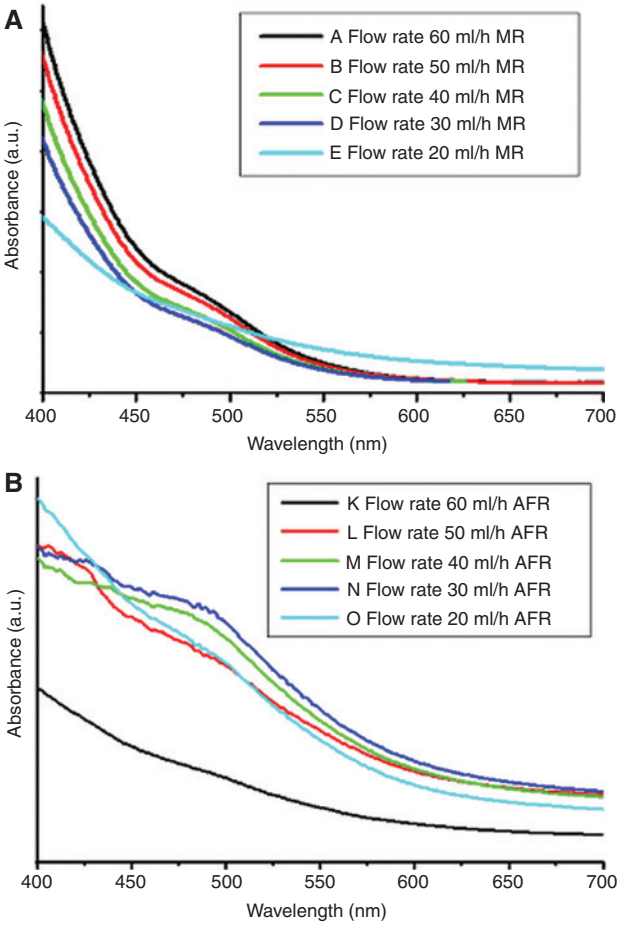

Figure 2: (A) UV absorption spectra of iron oxide NPs with varying flow rate in MR and (B) UV absorption spectra of iron oxide NPs with varying flow rate in the AFR™.

combination of larger number but smaller NPs, a larger concentration of iron oxide NPs is obtained in the reaction mixture which leads to an increase in the absorbance value of the sample. At higher flow rate, more turbulence favoring the formation of NPs is observed as compared to lower flow rate where agglomeration might take place.

Similarly, in the case of AFR™ reactor, colloidal iron oxide NPs were obtained as yellow brown colored precipitate formed due to iron reduction acceleration. As shown in Figure 2B, it was observed that the λ_{max} value obtained is between 480 and 490 nm for all cases at different flow rates in AFR™ in the presence of CTAB surfactant. The heart-shaped design in AFR™ gives superior mixing, however, the residence time is higher in the case of AFR™ as compared to the MR and hence the particle size was higher in the case of AFR™ as compared to the MR and also the PSD was more wider in the case of AFR™ as compared to the MR. Due to the higher residence time in AFR™ higher extent of crystal growth of NPs occurs after short nucleation time resulting in higher size and also wider distribution [53–56]. From the data obtained for the UV absorbance spectra and average particle size (Table 1), it was established that the iron oxide NPs prepared in AFR™ have higher particle size compared to that obtained in the case of the MR, attributed to higher residence time in AFR™.

3.3 Effects of feed flow rate on PSD of the obtained iron oxide nanoparticles in microreactor and AFR™

The effect of feed flow rate on the PSD of iron oxide NPs was studied using various flow rates (20–60 ml/h) at a constant reductant to precursor molar ratio (1 : 1) in the presence of surfactant (CTAB). As per the data shown in Figure 3A–E for the PSD and average particle size reported in Table 1, it can be established that the particle size deceases with an increase in the feed flow rate which is attributed to lower residence time [1, 57]. The minimum average particle size obtained in the case of spiral MR was 6.3 nm at higher flow rate of 60 ml/h and the PSD was also narrow in the range of 3.76–18.92 nm as reported in Figure 3A and Table 1. At the lower flow rate of 30 ml/h in the MR, wide size distribution was obtained over the range of 6.77–25.37 nm (Figure 3D and Table 1). Therefore, it can be established from the obtained data for the particle size analysis that larger residence time (lower flow rates) in the reactor results in the formation of larger sized nanoparticle. The observed trend is attributed to the larger residence time offering more time for agglomeration and crystal growth of particles resulting into larger particle size. It was also confirmed by TEM

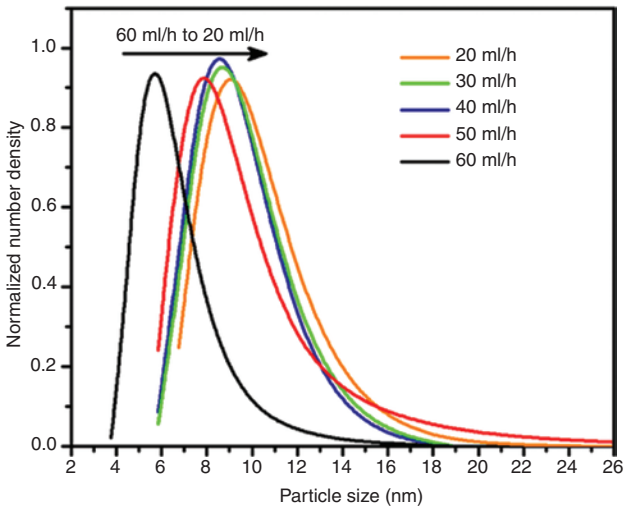

Figure 3: Particle size distribution (PSD) of iron oxide NPs in MR at 60, 50, 40, 30, and 20 ml/h flow rate.

images depicted in Figure 4A,B that at the flow rate of 50 ml/h used in the MR, the particle size obtained was in the range of ~3–8 nm (Figure 4A,B).

Similarly, the effect of feed flow rates on the particle size was studied at the same flow rates and constant molar ratio in AFR™ reactors. As depicted in Figure 5A–E and Table 1, average particle size of iron oxide NPs generally decreased with an increase in the flow rate with minimum size being obtained at the flow rate of 50 ml/h (Figure 5B). The uniform mixing obtained due to the unique heart shape design of Corning reactor played a significant role in the reduction of the particle size. At higher flow rates of 60 and 50 ml/h, narrow PSD over the range of 6.77–29.39 nm and 3.76–18.92 nm, respectively, was observed as depicted in Figure 5A,B and Table 1. On the other hand, at lower flow rate of 20 ml/h, wide PSD was observed over the range of 10.1–43.82 nm as depicted in Figure 5D and Table 1. It can also be established from the data depicted in Figure 5B that the average particle size is 6.64 nm for the flow rate 50 ml/h from PSD data due to initiation and nucleation of NPs (in AFR™) occurs faster at 50 ml/h than at 60 ml/h because particle size depends on nucleation process and residence time of NPs in reactor, which was also confirmed using the TEM image as represented in Figure 6, which showed that the particle size is over the range of ~2–8 nm.

3.4 Zeta potential analysis for particles obtained in microreactor and AFR

As per the data shown in Figure 7, it was observed for the case of spiral MR that as the flow rate reduced from

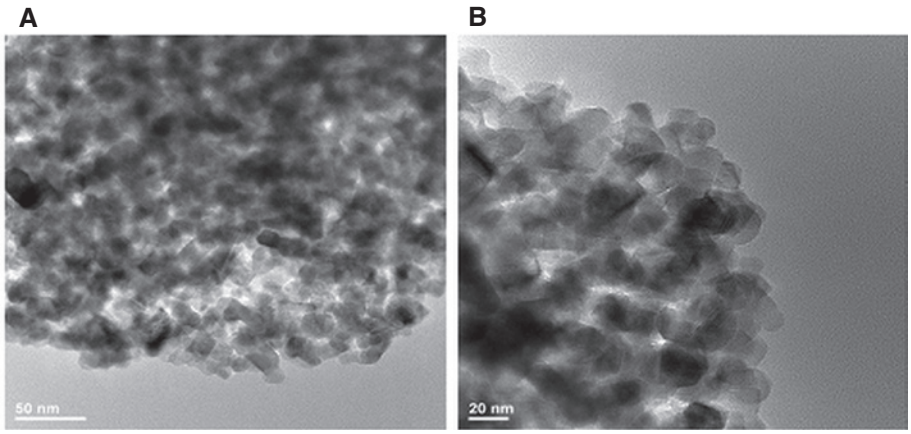

Figure 4: (A, B) Transmission electron microscopy image of iron oxide NPs synthesized in MR at 50 ml/h using CTAB as a surfactant. Scale bars: (A) 50 and (B) 20 nm.

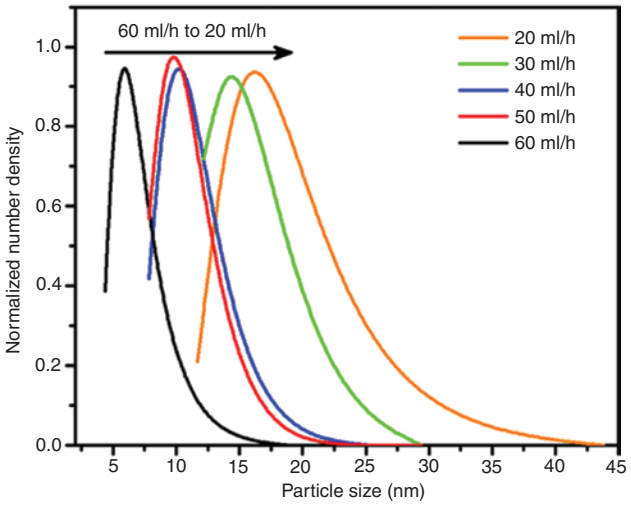

Figure 5: Particle size distribution of iron oxide NPs in AFR™ at 60, 50, 40, 30, and 20 ml/h flow rate.

60 ml/h to 40 ml/h, zeta potential value increased from 14.6 to 42.1 mV, which confirms more stability of formed NPs in homogenous solutions. However, at a very low flow rate of 30 and 20 ml/h, the observed zeta potential value is 37.2 and −0.06 mV which shows less stability of the formed NPs.

Similarly in the case of AFR™ reactor, reduction in the flow rate from 60 to 40 ml/h resulted in an increase in the zeta potential value from 0.046 and 22.0 mV confirming higher stability of NPs at optimum flow rates. At very low flow rates of 30 and 20 ml/h, the zeta potential values observed were 4.60 and 0.0806 mV, respectively, which confirmed less stability, similar to the case of spiral MR.

It is also important to understand that the zeta potential values were different in the two types of reactors used in the reactor indicating difference in the stability of the obtained NPs. The observed trends can be attributed to the

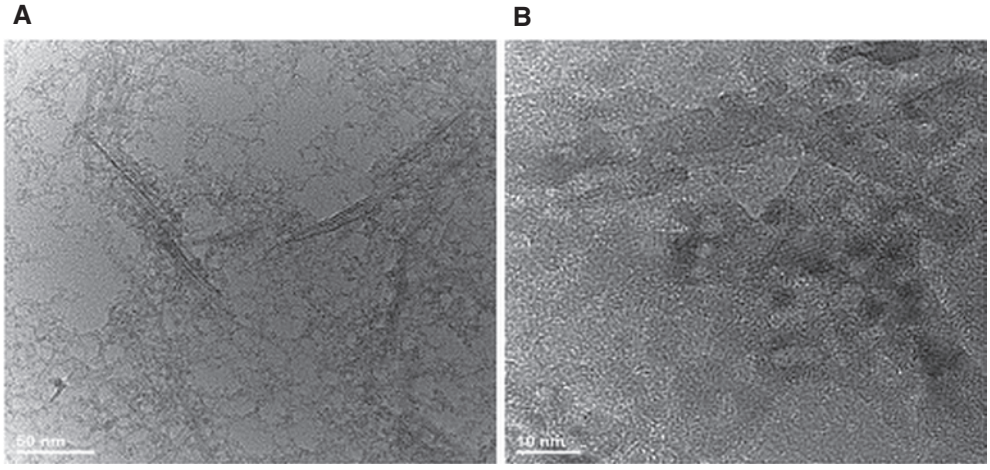

Figure 6: (A, B) TEM image of iron oxide NPs synthesized in AFR™ at 50 ml/h using CTAB as a surfactant. Scale bars: (A) 50 and (B) 10 nm.

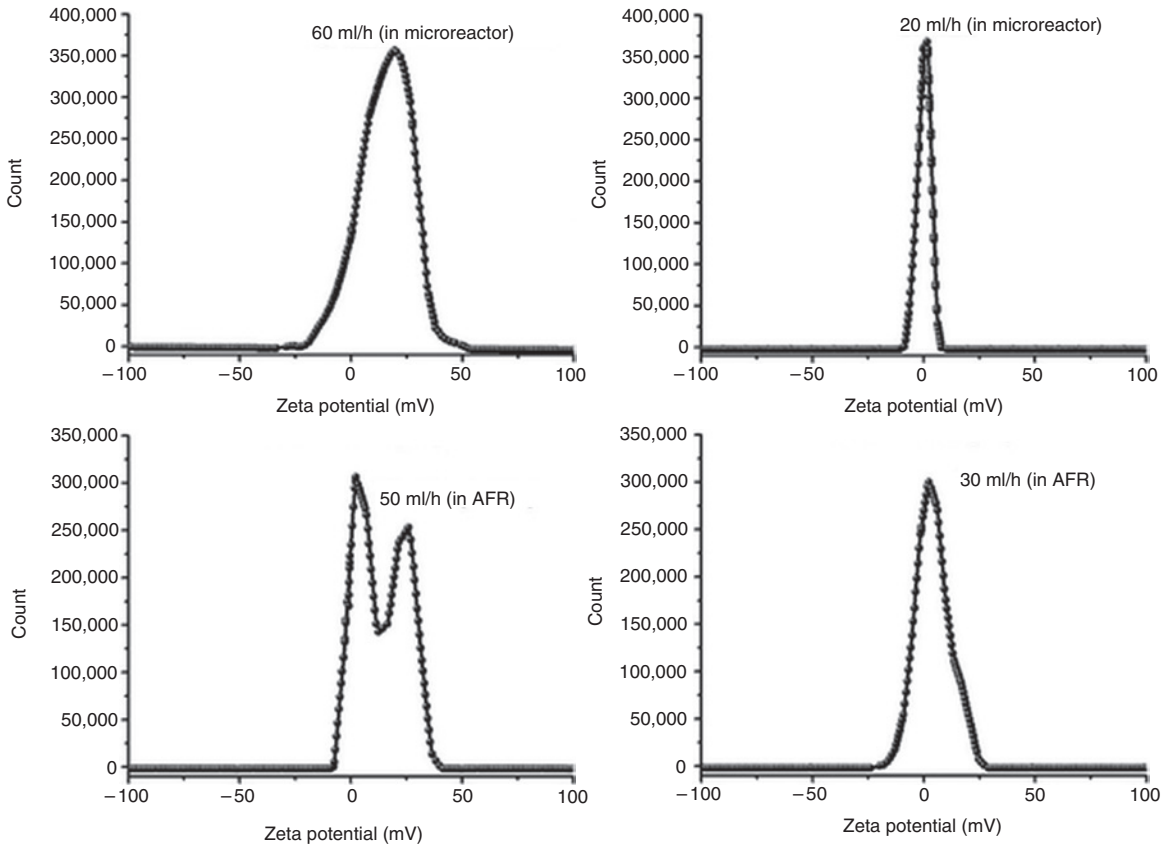

Figure 7: Zeta potential of iron oxide NPs in MR (top left) at 60 ml/h flow rate and (top right) at 20 ml/h flow rate. Zeta potential of iron oxide NPs in AFR™ (bottom left) at 50 ml/h flow rate and (bottom right) at 30 ml/h flow rate.

changes in the size (affected by the residence time) and shape (affected by the mixing pattern) for the obtained NPs. The changes in the mixing patterns and its intensity affect the nucleation, formation and growth of the iron oxide NPs, in turn, affecting the size and poly-dispersity of the obtained NPs. Further the mixing pattern in the reactor plays an important role in the process of nanoparticle formation in different types of reactors, affecting the particle size, PSD, and stability of iron oxide NPs which in turn affects the obtained zeta potential values [53, 57].

3.5 Stabilization of iron oxide nanoparticles using surfactant

The FTIR spectrum analysis for the iron NPs prepared in MR and AFR™ at a flow rate of 50 ml/h have been depicted in Figure 8 which clearly indicates that the formed iron oxide NPs were stabilized by surfactant, i.e. CTAB. The observed absorption bands are in the range of 450–740 cm^{-1} representing the Fe–O vibration band of iron oxide NPs [36]. The observed peaks at 523.7 and 503.44 cm^{-1} in MR (peak A)

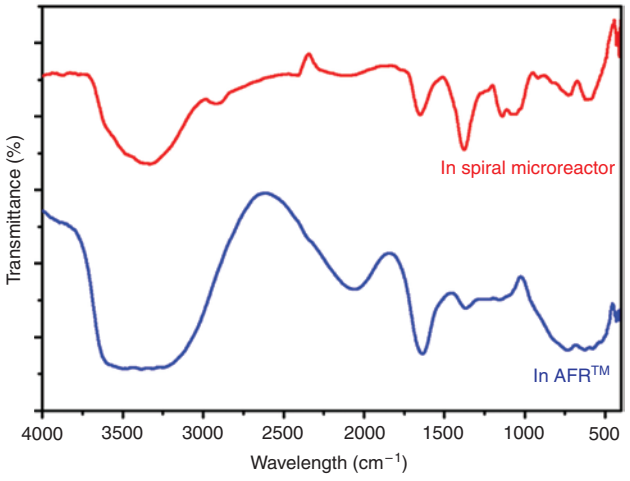

Figure 8: FTIR spectra of synthesized CTAB-coated iron oxide NPs in the MR and the AFR™.

and 611.45 cm^{-1} in the AFR reactor (peak B) were attributed to Fe–O band vibration of iron oxide (Fe_2O_3). In both reactors, the observed peaks at 1366.6 and 1378.18 cm^{-1} are attributed to C–N bond whereas the C–H bands stretching

vibration of CTAB are observed at the peaks of 3000 and 2909.7 cm^{-1} in MR and AFR™, respectively. The prominent peaks of N–H bond and O–H stretching show more stretching vibrations at 3235.7 and 3314.78 cm^{-1} and also the characteristic band of amide group ($–NH_2$) is observed at 1635.7 and 1650.16 cm^{-1} in MR and AFR, respectively (Figure 8) [58–60].

3.6 Effect of type of reactors and residence time on the formation of colloidal iron oxide nanoparticles

In the case of an MR, the average particle size was found to be less at a high flow rate of 60 ml/h (about 6.3 nm as depicted in Table 1). The particle size is less in the case of spiral MR attributed to the shorter residence time which gives higher rate of nucleation and slower growth rate. In the case of AFR™ reactor, at higher flow rates of 60 and 50 ml/h, the average particle sizes 10.5 and 6.64 nm were observed, respectively. At the lesser flow rate of 20 ml/h, the observed average particle size was larger (around 18.2 nm as reported in Table 1) in the AFR™. Narrow PSD was also observed in the case of MR compared to that in the AFR™. It is attributed to the lesser residence time observed in the case of MR as compared to the AFR™ (Table 1). The dimensions of the mixing zone and path length volume of the AFR™ are larger than that of the MR and hence in the case of AFR™ wide PSD was observed as compared with MR. Hence, it was established that the spiral MR will provide superior mixing of a precursor and a reducing agent for the formation of small size NPs.

3.7 XRD analysis

The crystallinity of the synthesized iron oxide NPs in MR was investigated by the XRD study. The obtained results for the XRD pattern have been depicted in Figure 9. The JCPDS file 019-0629 closely matched with the XRD pattern observed in this study showing the characteristic peaks at 2θ of 20.75, 31.71, 36.59, 38.98, 45.45, 53.49, 56.44, and 61.11 corresponding to face centered cubic phase of (111), (220), (311), (222), (400), (422), (511), and (440) planes, respectively. The presence of strong and sharp peaks of Fe_2O_3 crystals are attributed to the highly crystalline nature [60–62]. The average crystal size was estimated as 6.62 ± 0.5 nm from the sharp broad peak width of pure Fe_2O_3 NPs at (111) using the Debye-Scherrer equation (Figure 9), which is in good agreement with the particle size observed from TEM images (Figure 4A,B).

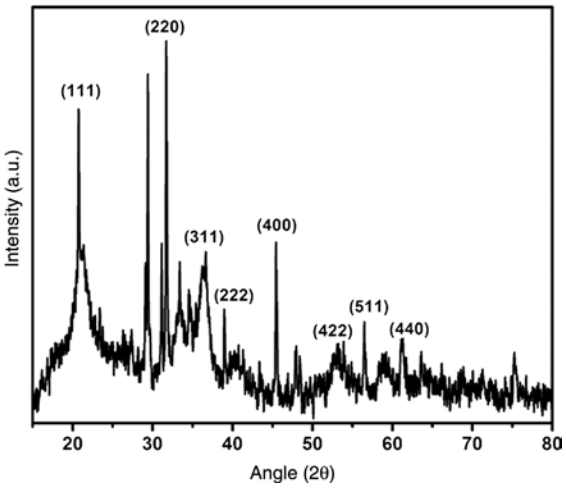

Figure 9: XRD pattern of synthesized iron oxide NPs in a MR.

3.8 Magnetic property analysis of iron oxide nanoparticles using ESR

Electron spin resonance (ESR) techniques were used to detect unpaired electrons and identify the magnetic characteristics as well as the purity of iron oxide NPs samples [63]. The ESR technique is also called as the electron paramagnetic resonance and the analysis works by two ways of without an external magnetic field (the internal electron spins randomly) and with applied external magnetic field where unpaired electron spins are arranged in parallel or anti-parallel, which then separate into two energy levels (E1 and E2). The observed phenomenon is also called the Zeeman effect/splitting [64]. The spectroscopic splitting factor (g) can be calculated using the relation

$$g = h\upsilon / \beta H \tag{4}$$

where h is the Planck's constant, υ is the applied microwave frequency (9.185 GHz), β is the Bohr magneton, and H is the resonance magnetic field [27, 65].

The ESR measurements were performed at constant temperature of $25°C \pm 3°C$. The magnetization ESR spectrum curves of iron NPs synthesized in the MR and advanced flow reactor have been shown in Figure 10A,B. The iron oxide NPs synthesized in the MR and AFR™ showed higher value of saturated magnetization. From the ESR spectra (Figure 10), it can be clearly seen that the symmetric resonance absorption peaks of iron NPs showed broad peak intensity at the room temperature with g-factor values equal to 2.05544 and 2.03421 (from Equation 4) corresponding to the magnetic field of 319.28 and 322.59 mT for MR and AFR™, respectively [14, 18, 66]. The g-factor value is nearly similar to the g-factor value

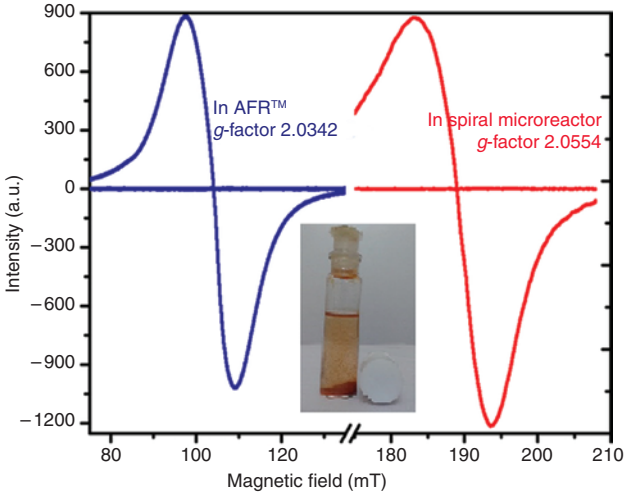

Figure 10: ESR spectrum of the synthesized iron oxide at room temperature in (red graph) MR and (blue graph) AFR™. Inset figures show suspended magnetic iron oxide NPs attracted by a magnet.

of free electron which is ~2.0023 and is consistent with the literature value reported for the superparamagnetic iron NPs [64, 67–69]. Inset in Figure 10 shows that the suspended magnetic iron oxide NPs in colloidal solution were attracted by the external magnetic field with the use of a permanent magnet. Mamani et al. [18] also reported similar results for the magnetometry of magnetic NPs at room temperature confirming Fe^{3+} ion interaction and the transition between the superparamagnetic and ferromagnetic behavior. The exchange interaction between spins aligned and extensions depend on the concentration of iron (Fe^{3+}) ions. The observed *g*-factor values are attributed to the super exchange interaction and also to the magnetic dipole interaction between NPs [27, 70].

4 Conclusions

In the present work, stable colloidal iron oxide NPs have been successfully prepared by co-precipitation and reduction method in both Y-type microchannel spiral copper tube MR and Corning AFR™. It has been demonstrated that the differences in the residence time and mixing patterns observed in these reactors have drastic effect on particle size and PSD of the obtained iron oxide NPs, which in turn also affects the stability and the magnetic properties. The use of capping agent, CTAB, helps in stabilizing the synthesized iron oxide NPs. The flow rate of reactants was observed to be the key parameter to decide the mean particle size as well as the size distribution of NPs. It has been established that the average particle size of iron oxide NPs decreased with an increase in the flow rate of the reactants. The average particle size of iron oxide NPs was observed to be around 6 nm for flow rate of 60 ml/h in MR and 50 ml/h in AFR™, respectively. The size distribution of the synthesized iron oxide NPs was over the range of 3 and 8 nm for the case of spiral MR and over the range of 2 and 8 nm for the case of AFR™ which were also confirmed from TEM images. The prepared iron oxide NPs showed super-paramagnetic behavior as confirmed by ESR spectrum analysis and studies based on the use of a permanent magnet. Overall the current work demonstrated efficient synthesis of the magnetic iron oxide NPs using two types of MRs and also establishing the efficacy of each type.

Acknowledgments: The authors gratefully acknowledge Corning Technologies for providing the facility to use Corning AFR™ and the Department of Electronic and Information Technology, Government of India for financial support.

Conflict of interest statement: The authors declare that there is no conflict of interest regarding the publication of this article.

References

[1] Wagner J, Kohler JM. *Nano Lett.* 2005, 5, 685–691.
[2] Sadiq M, Zamin G, Ilyas RM. *Modern Res. Catal.* 2014, 3, 12–17.
[3] Sastry M, Mukherjee P, Patra CR, Ghosh A, Kumar R. *Chem. Mater.* 2002, 14, 1678–1684.
[4] Kohler JM, Csaki A, Reichert J, Moller R, Straube W, Fritzsche W. *Sens. Actuators B* 2001, 76, 166–172.
[5] Henglein A. *Chem. Mater.* 1998, 10, 444–450.
[6] Chilkoti A, Nath N. *Anal. Chem.* 2002, 74, 504–509.
[7] Zhao CX, He L, Qiao S, Middelberg APJ. *Chem. Eng. Sci.* 2011, 66, 1463–1479.
[8] Wu W, He Q, Jiang C. *Nanoscale Res. Lett.* 2008, 3, 397–415.
[9] Babes L, Denizot B, Tanguy G, Le Jeune JJ, Jallet P. *J. Colloid Interf. Sci.* 1999, 212, 474–482.
[10] Khalil MI. *Arabian J. Chem.* 2015, 8, 279–284.
[11] Atkinson JD, Fortunato ME, Dastgheib SA, Rastom-Abadi M, Rood MJ, Suslick KS. *Carbon* 2011, 49, 587–598.
[12] Mohapatra M, Anand S. *Int. J. Eng. Sci. Technol.* 2010, 2, 127–146.
[13] Rivet C, Lee H, Hirsch A, Hamilton S, Lu H. *Chem. Eng. Sci.* 2011, 66, 1490–1507.
[14] Morales MA, Finotelli PV, Coaquira JAH, Rocha-Leao MHM, Diaz-Aguila C, Baggio-Saitovitch EM, Rossi AM. *Mater. Sci. Eng. C* 2008, 28, 253–257.
[15] Nan SS, Chao W, Zan ZZ, Long HY, Venkatraman SS, Chuan XZ. *Chin. Phys. B* 2014, 23, 1–19.
[16] Xu P, Zeng G, Huang D, Feng C, Hu S, Zhao M, Lai C, Wei Z, Huang C, Xie GX, Liu ZF. *Sci. Total Environ.* 2012, 424, 1–10.
[17] Wahajuddin SA. *Int. J. Nanomedicine* 2012, 7, 3445–3471.
[18] Mamani JB, Gamarra LF, de Souza Brito DE. *Mater. Res.* 2014, 17, 542–549.

[19] Chertok B, David A, Yang VC. *J. Controlled Release* 2011, 155, 393–399.
[20] Mahmoudi M, Sant S, Wang B, Laurent S, Sen T. *Adv. Drug Deliv. Rev.* 2011, 63, 24–46.
[21] Dissanayake NM, Current KM, Obare SO. *Int. J. Mol. Sci.* 2015, 16, 23482–23516.
[22] Hasany SF, Ahmed I, Rajan J, Rehman A. *Nanosci. Nanotechnol.* 2012, 2, 148–158.
[23] Abdulkadir I, Aliyu AB. *Afr. J. Pure Appl. Chem.* 2013, 7, 114–121.
[24] Yuvakkumar R, Elango V, Rajendran V, Kannan N. *Dig. J. Nanomater. Biostruct.* 2011, 6, 1771–1776.
[25] Behera SS, Patra JK, Pramanik K, Panda N, Thatoi H. *World J. Nano Sci. Eng.* 2012, 2, 196–200.
[26] Lee WB, Weng CH, Cheng FY, Yeh CS, Lei HY, Lee GB. *Biomed. Microdevices* 2009, 11, 161–171.
[27] Shahane GS, Zipare KV, Pant RP. *Magnetohydrodynamics* 2013, 49, 317–321.
[28] Azimi N, Rahimi M, Abdollahi N. *Chem. Eng. Process* 2015, 97, 12–22.
[29] Watts P, Wiles C. *Chem. Commun.* 2007, 2007, 443–467.
[30] Lavric ED, Woehl P. *Chem. Today* 2009, 27, 45–48.
[31] Jorda J, Vizza A. *Speciality Chem. Mag.* 2012, 33, 19–21.
[32] Singh A, Malek CK, Kulkarni SK. *Int. J. Nanosci.* 2010, 9, 93–112.
[33] Calabrese GS, Pissavini S. *AIChE J.* 2011, 57, 828–834.
[34] Woitalka A, Kuhn S, Jensen KF. *Chem. Eng. Sci.* 2014, 116, 1–8.
[35] Gemoets HPL, Su Y, Shang M, Hessel V, Luque R, Noel T. *Chem. Soc. Rev.* 2016, 45, 83–117.
[36] Darr JA, Poliakoff M. *Chem. Rev.* 1999, 99, 495–541.
[37] Koo B, Xiong H, Slater MD, Prakapenka VB, Balasubramanian M, Podsiadlo P, Johnson CS, Rajh T, Shevchenko EV. *Nano Lett.* 2012, 12, 2429–2435.
[38] Du X, Wang C, Chen M, Jiao Y, Wang J. *J. Phys. Chem. C* 2009, 113, 2643–2646.
[39] Lin S, Shen C, Lu D, Wang C, Gao HJ. *Carbon* 2013, 53, 112–119.
[40] Long NV, Teranishi T, Yang Y, Thi CM, Cao Y, Nogami M. *Int. J. Metall. Mater. Eng.* 2015, 1, 119–136.
[41] Ugelstad J, Berge A, Ellingsen T, Schmid R, Nilsen TN, Mork PC, Stenstad P, Hornes E, Olsvik O. *Prog. Polym. Sci.* 1992, 17, 87–161.
[42] Liu Y, Gao Y, Xu C. *Chin. Phys. B* 2013, 22, 097503–097511.
[43] Lu AH, Salabas EL, Schuth F. *Angew. Chem. Int. Ed.* 2007, 46, 1222–1244.
[44] Shi JB, Lee CW, Guo JW, Cheng MJ, Wu C, Chen CJ, Chen YC, Lin YT, Change CC. *Mater. Lett.* 2007, 61, 5268–5270.
[45] Wang YXJ, Xuan S, Port M, Idee JM. *Curr. Pharm. Des.* 2013, 19, 6575–6593.
[46] Alagiri M, Hamid SBA. *J. Sol-Gel Sci. Technol.* 2015, 74, 783–790.
[47] Wu W, Wu Z, Yu T, Jiang C, Kim WS. *Sci. Technol. Adv. Mater.* 2015, 16, 023501–023543.
[48] Kim J, Park S, Lee J E, Jin SM, Lee JH, Lee IS, Yang I, Kim JS, Kim SK, Cho MH, Hyeon T. *Angew, Chemie* 2006, 118, 7918–7922.
[49] Yu J, Huang D, Yousaf MZ, Hou Y, Gao S. *Chin. Phys. B* 2013, 22, 027506.
[50] Sonawane SH, Bari ML, Suryawanshi PL, Narkhede JS, Mishra S, Bhanvase BA. *Chem. Eng, Technol.* 2015, 38, 1765–1773.
[51] Khan Z, Hussain JI, Kumar S, Hashmi AA, Malik MA. *J. Biomater. Nanobiotechnol.* 2011, 2, 390–399.
[52] Laurent S, Forge D, Port M, Roach A, Robic C, Elst LV, Muller RN. *Chem. Rev.* 2008, 108, 2064–2110.
[53] Sugano K, Uchida Y, Ichihashi O, Yamada H, Tsuchiya T, Tabata O. *Microfluid Nanofluid* 2010, 9, 1165–1174.
[54] Winterton JD, Myers DR, Lippmann JM, Pisano AP, Doyle FM. *J. Nanoparticle Res.* 2008, 10, 893–905.
[55] Sun Y. *Chem. Soc. Rev.* 2013, 42, 2497–2511.
[56] Sharada S, Suryawanshi PL, Rajesh Kumar P, Gumfekar SP, Narsaiah TB, Sonawane SH. *Colloids Surf A Physicochem. Eng. Asp.* 2016, 498, 297–304.
[57] Petschacher C, Eitzlmayr A, Besenhard M, Wagner J, Barthelmes J, Schnurch AB, Khinast JG, Zimmer A. *Polym. Chem.* 2013, 4, 2342–2352.
[58] Khoshnevisan K, Barkhi M, Zare D, Davoodi D, Tabatabaei M. *Metal-Org. Nano-Met. Chem.* 2012, 42, 644–648.
[59] Kumar K, Nightingale A, Krishnadasan S, Kamaly N, Wylenzinska-Arridge M, Zeissler K, Branford W, Ware E, deMello AJ, deMello JC. *J. Mater. Chem.* 2012, 22, 4704–4708.
[60] Salem NM, Awwad AK. *Nanosci. Nanotechnol.* 2013, 3, 35–39.
[61] Yu BY, Kwak SY. *J Mater Chem.* 2010, 20, 8320–8328.
[62] Bagherzadeh M, Amrollahi MA, Makizadeh S. *RSC Adv.* 2015, 5, 105499–105506.
[63] Kus M, Ozel F, Varal N, Ersoz M. *Prog Electromag. Res.* 2013, 134, 509–524.
[64] Fukuchi T. *Dr. Sebastiano D'Amico (Ed.) In-Tech Publication* 2012, ISBN: 978-953-307-991-2.
[65] Chetri P, Choudhury B, Choudhury A. *J. Mater Chem. C* 2014, 2, 9294–9302.
[66] Herring MP, Khachatryan L, Dellinger B. *World Acad. Sci. Eng. Technol.* 2015, 9, 804–812.
[67] Koseoglu Y, Aktas B. *Phys. Stat. Sol. (c)* 2014, 1, 3516–3520.
[68] ur Rahman O. *Mater Chem. Phys.* 2012, 132, 196–202.
[69] Mitsumata C, Tomita S, Hagiwara M, Akamatsu K. *J Phys. Condens Matter* 2010, 22, 016005–016014.
[70] Ki L, Li G, Smith RL, Inomata H. *Chem. Mater* 2000, 12, 3705–3714.

Bionotes

Prashant L. Suryawanshi

Prashant L. Suryawanshi is currently working as a research scholar at Department of Chemical Engineering, National Institute of Technology, Warangal, India. He completed his BTech. and MTech. in chemical engineering at the Department of Chemical Technology, North Maharashtra University, Jalgoan, India in 2011 and 2013, respectively. His areas of interest are nanotechnology, micro-reactors, fuel cell technology, and catalyst synthesis.

Shirish H. Sonawane

Shirish H. Sonawane is currently working as an associate professor at Chemical Engineering Department, National Institute of Technology Warangal, Telengana, India. His research interests are focused on synthesis of hybrid nanomaterials, cavitation-based inorganic particle synthesis, sonochemical synthesis of nanolatex, process intensification, and microreactors for nanoparticle production. Dr. Sonawane has published more than 100 research papers in reputed journals, eight book chapters, and has six Indian patent applications to his credit.

Bharat A. Bhanvase

Bharat A. Bhanvase is currently working as an associate professor at Chemical Engineering Department, Laxminarayan Institute of Technology, RTM Nagpur University, Nagpur, Maharashtra, India. His research interests are focused on wastewater treatment, cavitation-based nanomaterials and nanocomposites, process intensification, microfluidics, and nanofluids. He has published 40 articles in international journals, four in national journals, and 19 book chapters. He is a recipient of the Young Scientist Award for Science and Engineering Research Board, New Delhi.

Muthupandian Ashokkumar

Muthupandian Ashokkumar (Ashok) is a physical chemist who specializes in sonochemistry, teaches undergraduate and post-graduate chemistry and is a senior academic staff member of the School of Chemistry, University of Melbourne. Ashok is a renowned sonochemist who has developed a number of novel techniques to characterize acoustic cavitation bubbles. He has edited/co-edited several books and special issues for journals and published approximately 320 refereed papers in high impact international journals and books.

Makarand S. Pimplapure

Makarand S. Pimplapure is currently working as an application development manager at Corning. His research interests are focused on process modeling, reaction engineering, conceptual process design, flow chemistry/microrecator technology, and process intensification. He completed his Ph.D. in chemical engineering at Universiteit Twente in 2006.

Parag R. Gogate

Parag R. Gogate is currently working as an associate professor at Institute of Chemical Technolgy (ICT), Matunga, Mumbai, India. Dr. Gogate has been a versatile chemical engineer with outstanding research work based on the use of alternate energy sources for process intensification, wastewater treatment, and synthesis of nanomaterials. Dr. Gogate has to his credit 225 publications in international, highly reputed journals along with over 9857 citations (h-index of 53). He is also the author of 15 book chapters.